JGR Atmospheres

RESEARCH ARTICLE
10.1029/2025JD043563

Special Collection:
Southern Ocean clouds, aerosols, precipitation and radiation

Comparison of Cloud and Radiation Measurements to Models Over the Southern Ocean at Escudero Station, King George Island

Penny M. Rowe[1], Xun Zou[2], Irina Gorodetskaya[3], Robert A. Stillwell[4], Raul R. Cordero[5], David Bromwich[6], Zhenhai Zhang[2], F. Martin Ralph[2], and Steven Neshyba[7]

[1]NorthWest Research Associates, Seattle, WA, USA, [2]CW3E, Scripps Institution of Oceanography, University of California San Diego, La Jolla, CA, USA, [3]CIIMAR | Interdisciplinary Centre of Marine and Environmental Research, University of Porto, Porto, Portugal, [4]Earth Observing Lab, NSF National Center for Atmospheric Research, Boulder, CO, USA, [5]University of Santiago of Chile, Santiago, Chile, [6]Polar Meteorology Group, Byrd Polar and Climate Research Center, The Ohio State University, Columbus, OH, USA, [7]University of Puget Sound, Tacoma, WA, USA

Abstract Clouds and radiation play an important role in warming events over the Southern Ocean (SO). Here we evaluate European Center for Medium-Range Weather Forecasts Reanalysis version 5 (ERA5) and Polar Weather Research Forecast (PWRF) output through comparison to surface-based measurements of clouds, radiation, and the atmospheric state over the SO during 2017–2023 at Escudero Station (62.2°S, 58.97°W) on King George Island. ERA5 mean monthly downward shortwave (DSW) radiative fluxes are found to be 38–50 W m^{-2} higher than observations in summer, whereas ERA5 mean monthly downward longwave (DLW) is biased by −18 to −22 W m^{-2} in summer and −16 W m^{-2} on average over the year. Comparisons of temperature, humidity, and lowest-cloud base heights between ERA5 and observations rule these factors out as large contributors to the DLW flux biases. The similarity between observed DLW cloud forcing distributions for atmospheric columns containing low-level liquid and ice-only clouds suggests limited influence of cloud phase errors on DLW biases. Thus the most likely explanation for DLW flux biases in ERA5 is underestimated cloud optical depth, which is also consistent with DSW flux biases. Similar biases in ERA5 are found during atmospheric river (AR) events. By contrast, PWRF flux bias magnitudes are much smaller during AR events (−12 W m^{-2} for DSW and −2 W m^{-2} for DLW). After bias correction, ERA5 monthly average net cloud forcing over 2017–2023 is found to be a minimum of −107 W m^{-2} in January and a maximum of 65 W m^{-2} in June.

Plain Language Summary Clouds play an important role in warming events on the Antarctic Peninsula and over the Southern Ocean due to their interaction with infrared and solar radiation. The challenge of properly modeling clouds in this remote region leads to biases in climate and weather forecasting models. Here we evaluate two widely used models: the Polar Weather Research Forecasting model, or PWRF, and the European Center for Medium-Range Weather Forecasts Reanalysis version 5 model, or ERA5. We compared outputs from the models to measurements made on King George Island in the Southern Ocean, north of the Antarctic Peninsula, during 2017–2023. We find that PWRF agreed fairly well with observations overall, although there was a lot of variability between them. By contrast, compared to measurements ERA5 was found to predict more sunlight and less infrared light making it to the surface. It seems likely that the biases are caused by ERA5 not modeling enough clouds, since clouds reflect sunlight and trap infrared light. Clouds cause an overall cooling in the summer and warming in the winter, and the biases in ERA5 lead to underestimating the fraction of the year when clouds cause an overall warming by about 2 and a half weeks.

Key Points:

- ERA5 overestimates monthly mean shortwave downward flux by up to 50 W m^{-2} and underestimates longwave by 16 W m^{-2} in the Southern Ocean
- Bias-corrected ERA5 monthly average net cloud forcing over the Southern Ocean (62.2°S, 58.97°W) ranges from −107 to 65 W m^{-2}
- During strong summer atmospheric rivers in the Southern Ocean, downward radiation biases at the surface are larger in ERA5 than PWRF

Supporting Information:

Supporting Information may be found in the online version of this article.

Correspondence to:

P. M. Rowe,
penny@nwra.com

Citation:

Rowe, P. M., Zou, X., Gorodetskaya, I., Stillwell, R. A., Cordero, R. R., Bromwich, D., et al. (2025). Comparison of cloud and radiation measurements to models over the Southern Ocean at Escudero Station, King George Island. *Journal of Geophysical Research: Atmospheres*, *130*, e2025JD043563. https://doi.org/10.1029/2025JD043563

Received 6 FEB 2025
Accepted 3 JUL 2025

Author Contributions:

Conceptualization: Penny M. Rowe, Xun Zou, Irina Gorodetskaya
Data curation: Penny M. Rowe, Robert A. Stillwell
Formal analysis: Penny M. Rowe, Xun Zou, Irina Gorodetskaya, Robert A. Stillwell
Funding acquisition: Penny M. Rowe, Raul R. Cordero, F. Martin Ralph, Steven Neshyba
Investigation: Penny M. Rowe
Methodology: Penny M. Rowe, Xun Zou, Zhenhai Zhang
Project administration: Penny M. Rowe

1. Introduction

Over the Southern Ocean (SO) and Antarctic Peninsula (AP), low clouds are ubiquitous and have a strong impact on the surface energy budget (Bodas-Salcedo et al., 2014; Gorodetskaya et al., 2023; Hu et al., 2010; Huang et al., 2012; Mace et al., 2009; McFarquhar et al., 2021; P. M. Rowe et al., 2025d; Tansey et al., 2023; Zou et al., 2023). Because of these strong radiative impacts, cloud properties play an important role in regional climate. For example, increases in cloud amount were implicated in downward longwave radiation increases that explain more than 70% of surface warming over the AP during 1950–2020 (Sato & Simmonds, 2021). Cloud

Visualization: Penny M. Rowe, Xun Zou, Robert A. Stillwell
Writing – original draft: Penny M. Rowe
Writing – review & editing: Penny M. Rowe, Xun Zou, Robert A. Stillwell, Raul R. Cordero, David Bromwich, Zhenhai Zhang, Steven Neshyba

radiative impacts have been shown to play a role in sea ice reduction, particularly during atmospheric river events (Liang et al., 2022), which often transport large amounts of moisture and heat from lower latitudes, and in sea ice advance in the inner region of the Antarctic sea-ice zone, which is predominantly driven by radiatively controlled freezing (Himmich et al., 2023). In addition, by reflecting shortwave radiation before it reaches the sea surface, clouds significantly reduce the radiative impact of sea ice loss on the surface energy budget (Alkama et al., 2020).

The effects of clouds on the surface energy budget are complicated by competing radiative effects: clouds reduce the incoming shortwave radiation and enhance the longwave radiation. The magnitudes of changes to the shortwave and longwave radiative components depend on cloud properties (Gilbert et al., 2020; Lubin et al., 2020; P. M. Rowe et al., 2020), as well as aerosols, infrared-active gases such as water vapor (Cox et al., 2015), solar elevation, and surface albedo. Solar elevation in turn depends on latitude, time of day, and season. As an example, over the summertime SO, where surface albedo is low and solar elevations can be large, shortwave radiation plays a dominant role (P. M. Rowe et al., 2025d; Trenberth & Fasullo, 2010; Zou et al., 2023), whereas in winter longwave radiation dominates (P. M. Rowe et al., 2025d).

These complex dependencies present significant challenges for accurately modeling the surface energy budget in climate and weather models. One bias common to many climate, weather forecasting, and reanalysis models is the overprediction of the amount of shortwave radiation absorbed by the SO (Bodas-Salcedo et al., 2012, 2014; Hyder et al., 2018; Naud et al., 2014; Trenberth & Fasullo, 2010), leading to model errors in ocean temperature and storm track positions (Bodas-Salcedo et al., 2014), the location of the midlatitude jet (Ceppi et al., 2012), meridional energy transport (Mason et al., 2014), tropical circulation and rainfall (Ceppi et al., 2012; Hwang & Frierson, 2013), and future climate predictions (Bodas-Salcedo et al., 2012). These biases have been attributed to underestimating cloud amounts, particularly for low clouds (Bodas-Salcedo et al., 2014; McFarquhar et al., 2021), and to underestimating the amount of supercooled liquid in SO clouds (Bodas-Salcedo et al., 2014; Kay et al., 2016; McFarquhar et al., 2021; Silber et al., 2019). Similarly, deficits in downwelling longwave radiation are common in these models. For example, European Center for Medium-Range Weather Forecasts Reanalysis version 5 (ERA5) downwelling longwave fluxes were found to be biased low by about 50 W m^{-2} for marine air masses year-round compared to observations at McMurdo Station, which was attributed to insufficient supercooled liquid clouds (Silber et al., 2019). North of the sea ice edge at 54.08°S, 89.67°W biases of −20 W m^{-2} in ERA5 were implicated in anomalously large predictions of sea-ice extent (Cerovecki et al., 2022).

Comparisons with measurements are key to understanding and improving these model biases. Here we evaluate how well ERA5 and the Polar Weather Research Forecasting (PWRF) model capture cloud and atmospheric properties over the SO. This evaluation is done through comparison to measurements of clouds and radiation made between 2017 and 2023 over the SO at Escudero Station (62.2°S, 58.97°W), on King George Island, situated just north of the AP. This location is near the northern edge of the Antarctic sea ice zone, where sea ice expansion is sensitive to the downward longwave radiative flux (Cerovecki et al., 2022). Moreover, the circumpolar westerly winds from the South Pacific Ocean impact King George Island, making the measurements broadly representative of this high latitude area. The measurements, which contributed to the Year of Polar Prediction—Southern Hemisphere (YOPP-SH; Bromwich et al., 2020), are unique in that they have longer duration than typical ship cruises or other campaigns. They are described by P. M. Rowe et al. (2025d) and have been used in a variety of case studies (Chyhareva et al., 2021; Gorodetskaya et al., 2023; P. M. Rowe et al., 2025d; Zou et al., 2023). Measurement and model results are used to characterize clouds and radiation and their interactions seasonally and during atmospheric river events.

2. Measurements and Models

2.1. Measurements at Escudero Station on King George Island

Measurements made at Escudero Station were described in P. M. Rowe et al. (2025d) and are therefore described only briefly here. Pyranometer and pyrgeometer instruments were used to measure downwelling shortwave (DSW) and downwelling longwave (DLW) fluxes. Mini micropulse lidar (miniMPL) data were collected and processed following the method of Stillwell et al. (2018), with differences as described in P. M. Rowe et al. (2025d). Cloud observations (pixels) on a two-minute time scale and 30 m vertical scale were classified as liquid for measured depolarization below 10% (for polarization errors not exceeding 1%) and otherwise as ice (for errors below 5%). These were used to determine cloud base heights. Following Stillwell et al. (2018) the atmospheric column was classified at each time step as clear, liquid-containing, containing only ice, or containing

Table 1
Measurements From Escudero Station on King George Island Used in This Work, Including Downwelling Shortwave (DSW) and Downwelling Longwave (DLW) Flux, Mini Micropulse Lidar (miniMPL) Cloud Measurements, Balloon-Borne Temperature and Humidity, and Surface Meteorology

Measurement	Date ranges	Measurement frequency
DSW flux	Jan. 2017–Aug. 2023	1 min
DLW flux	Dec. 2017–Aug. 2023	1 min
miniMPL	Summer 2017-2023 Autumn 2018–2020, 2022, 2023 Winter 2022, 2023 Spring 2017–2019, 2022	2 min
Upper air Temperature and Humidity	Summers 2017–2019, 2022, 2023 Autumn/Winter 2022, 2023 Spring 2017–2019, 2022	0–2 per day

water of unknown phase. If the Lidar signal was attenuated within the first 30 m, the column was classified as obscured. For these time periods it was assumed that a cloud existed, as discussed in P. M. Rowe et al. (2025d). These cases were categorized as containing clouds with unknown bases. Balloon-borne radiosondes were used to measure upper air pressure, temperature, humidity, and winds from the surface to approximately 20 km.

Table 1 summarizes the date ranges and frequency of these measurements. More details regarding the time periods of radiative flux, miniMPL, and radiosonde measurements are given in P. M. Rowe et al. (2025d). Throughout this work, we refer to the timeframe as 2017 to 2023 for brevity; however, as indicated in the table, measurements past Aug. 2023 were not used.

2.2. ERA5

This study makes use of a variety of reanalysis products from ERA5 (Hersbach et al., 2020), including vertical temperature and humidity profiles, cloud base heights, and surface DLW and DSW radiative fluxes for the scene-view and for clear skies. Hourly and monthly ERA5 data were obtained at 0.25-degree horizontal resolution at 62.25°S and 59.0°W, the closest grid point to Escudero Station (62.20°S, 58.97°W). Temperature and humidity profiles are provided by ERA5 at 37 pressure levels; here we use the first 36 pressure levels, which extend from 1,000 to 2 hPa.

2.3. PWRF

PWRF is a regional numerical weather prediction model developed and maintained by the Polar Meteorology Group of the Byrd Polar and Climate Research Center at The Ohio State University (Bromwich et al., 2013). PWRF revises the physical package of the standard WRF specifically for polar regions, incorporating improvements in sea ice representation and heat transfer processes through the snowpack (Hines et al., 2015). Previous studies confirm PWRF's skill in reliably simulating near-surface conditions, including surface pressure, wind, temperature, and surface energy balance (Deb et al., 2016; Gorodetskaya et al., 2023; Wille et al., 2024; Zou et al., 2023). PWRF V4.3.3 was used to provide high-resolution (as fine as 1.2 km) model simulations over the AP. A high-resolution topography data set, the Reference Elevation Model of Antarctica (REMA), and observed surface albedo from the Moderate Resolution Imaging Spectroradiometer (MODIS) are included in the input data to improve the surface description (Corbea-Pérez et al., 2021; Howat et al., 2019). The Morrison-Milbrandt P3 scheme (Morrison & Milbrandt, 2015) was selected for this study as it has been shown to produce more liquid cloud water compared to other schemes over West Antarctica, bringing the cloud liquid water amount into better agreement with Antarctic observations (Hines et al., 2019, 2021). Other PWRF model settings used in this study are the same as those given in Table 1 of Zou et al. (2023). Figure 1 shows the locations of the three domains used; Escudero Station is indicated with the purple dot in domain 3.

3. Methods

3.1. Cloud Amount and Base Altitude

To calculate the fraction of time when clouds were present according to ERA5 for comparison to the miniMPL measurements, clouds were assumed to exist whenever a cloud base height was reported in the ERA5 hourly data.

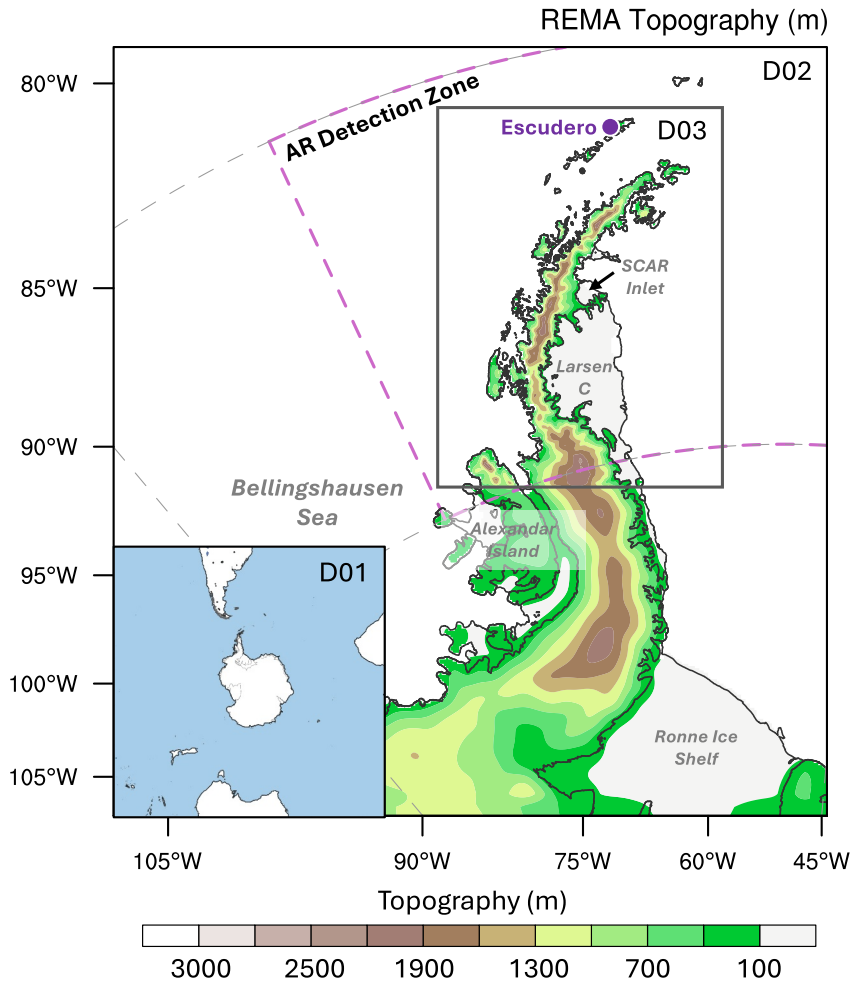

Figure 1. Map of the Antarctic Peninsula showing the location of Escudero Station as well as domains 2 and 3 (D02 and D03) used in PWRF and the region used for atmospheric river detection (purple dashed line). The inset panel shows domain 1 (D01), the greater Antarctic region. Topography (colors; m) is based on elevation information from the Reference Elevation Model of Antarctica (REMA; Howat et al., 2019).

This cloud mask was then used for seasonal and annual averages. For the miniMPL, the fractions of each day when the atmospheric column was clear or cloudy were first calculated and then monthly averages were calculated from them, as described in P. M. Rowe et al. (2025d).

Cloud-base altitudes for the lowest cloud layers were determined from the two-minute resolution miniMPL data. Because the miniMPL laser is attenuated by thick clouds, cloud tops and upper layer clouds were not reliably observed. The temperatures corresponding to the cloud base heights were determined using ERA5 hourly temperature profiles interpolated to miniMPL sampling times.

3.2. Temperature and Humidity Profiles

To compute average temperature and humidity profiles from ERA5 over the entire study period (2017–2023), monthly averages at each ERA5 pressure level at the closest grid point to Escudero Station were used.

For comparing ERA5 profiles to in situ radiosonde measurements, measured temperature and humidity profiles were interpolated to the ERA5 pressure levels from 1,000 to 30 hPa. During times when the surface pressure was less than 1,000 hPa, averages and differences excluded the 1,000 hPa level. ERA5 hourly data were selected at the closest grid point to Escudero Station and the closest times to the soundings (Differences for ERA5 profiles interpolated in space and time were found to be minimal.)

Table 2
Strong Atmospheric River (AR) Events Identified During Summers Within 2017–2023 Over the Antarctica Peninsula, Including Duration (Length), Scale, and Concurrent Radiosoundings (Sondes)

				Shortwave bias (W m^{-2})		Longwave bias (W m^{-2})		Total bias (W m^{-2})	
Date	Length (days)	AR scale[b]	Sondes (#)	ERA5	PWRF	ERA5	PWRF	ERA5	PWRF
2018/02/21	3	AR1	0	28.4	1.8	−16.7	−7.5	11.8	−5.7
2019/02/04	2	AR2	3	62.9	−3.1	−13.6	−5.1	49.3	−8.1
2020/02/04	7	AR3	0	4.2	−48.3	−6.9	12.0	−2.6	−36.3
2021/02/08	7	AR3	0	40.1	1.9	−18.0	−9.3	22.0	−7.5
2021/02/27	3	AR2	0	−52.9	−10.9	−17.4	−5.1	−70.2	−16.0
2021/12/08	3	AR2	0	34.1	−22.6	−10.3	−1.9	23.7	−24.5
2021/12/17	3	AR3	0	59.1	41.8	−16.3	−11.0	42.8	30.8
2022/01/19	3	AR2	1	48.2	−17.5	−9.7	−2.2	38.5	−19.7
2022/02/01	3	AR2	2	76.7	9.0	−27.9	−1.1	48.9	7.9
2022/02/07[a]	3	AR3	5	48.5	−23.5	−31.0	−2.6	17.5	−26.2
2022/02/20	5	AR2	8	30.7	−25.9	−16.0	−2.5	14.7	−28.5
Mean, Summer ARs	3.8	AR2.3	1.7	30.9	−12.3	−15.5	−2.3	15.3	−14.6

Note. Also shown are the biases in mean shortwave downwelling flux, longwave downwelling flux, and total downwelling flux (shortwave + longwave) for ERA5 and PWRF, based on comparisons to measurements made at Escudero Station. Means of radiation biases over all AR time periods listed, except as noted, are shown in the final row. [a]For this event, means of radiation biases were calculated over the period from 2022/02/06 00:00 UT to 2022/02/07 21:00 UT because PWRF runs started on 2022/02/06 and there was a gap in the measurements after 2022/02/07 21:00 UT. [b]The Polar AR scale was developed by the Center for Western Weather and Water Extremes (CW3E) to categorize the strength of ARs based on their maximum IVT and duration at a specific location (Zhang et al., 2024).

For comparing PWRF profiles to in situ radiosonde measurements, PWRF temperature and relative humidity profiles were interpolated to the latitude/longitude of Escudero Station, the sounding times, and the ERA5 pressure levels from 1,000 to 30 hPa. The PWRF model was only run during times when strong ARs were identified. Thus comparisons between PWRF profiles and radiosoundings were only made during time periods when strong AR conditions prevailed and when radiosondes were launched, leading to comparisons of 38 profiles, as shown in the first four columns of Tables 2 and 3 (the remaining columns are discussed in Section 4).

Table 3
Strong Atmospheric River (AR) Events Identified During Fall and Winters Within 2017–2023 Over the Antarctica Peninsula, Including Duration (Length), Scale, and Concurrent Radiosoundings (Sondes)

				Shortwave bias (W m^{-2})		Longwave bias (W m^{-2})		Total bias (W m^{-2})	
Date	Length (days)	AR scale	Sondes (#)	ERA5	PWRF	ERA5	PWRF	ERA5	PWRF
2022/05/11	4	AR1	8	1.4	0.4	−21.0	−15.5	−19.6	−15.0
2022/06/02	5	AR1	5	0.8	−0.1	−15.1	−2.5	−14.3	−2.5
2022/07/14	5	AR2	3	−0.2	−1.3	−10.0	3.8	−10.2	2.4
2022/07/26	4	AR1	0	−3.8	−4.9	−10.5	−4.4	−14.2	−9.3
2022/08/21[a]	9	AR2	3	6.6	5.4	−20.9	−10.6	−14.3	−5.2
Mean, Fall/Winter ARs	5.4	AR1.4	3.8	2.0	0.9	−16.3	−6.3	−14.3	−4.3

Note. Also shown are the biases in mean shortwave downwelling flux, longwave downwelling flux, and total downwelling flux (shortwave + longwave) for ERA5 and PWRF, based on comparisons to measurements made at Escudero Station. Means of radiation biases over all AR time periods listed, except as noted, are shown in the final row. For the cases shown, there was a cluster of ARs and the highest scale during that cluster is listed. [a]There were gaps in the measurements of about a day near the beginning and ending of the AR event; these were excluded from all means.

3.3. Downwelling Radiative Fluxes

When averaging fluxes over AR events, integer numbers of days were used so that shortwave averages included full diurnal cycles (except for ARs on 2022/02/07 and 2022/08/21, when measurements were missing during the event). For categorizing DLW fluxes by miniMPL atmospheric column classification, DLW fluxes were interpolated from the 1-min temporal sampling grid of the flux data to the 2-min temporal resolution used for the miniMPL measurements. For comparing monthly averages of measured DLW and DSW fluxes to ERA5 monthly averages, measured DLW and DSW fluxes were first averaged hourly, then monthly. This was done for two sets of ERA5 DLW and DSW fluxes: The first set included all ERA5 data for the time period, whereas the second set only included hourly averages when measurements were made. Clear-sky DLW fluxes were calculated at radiosonde times as described in P. M. Rowe et al. (2025d).

3.4. Cloud Forcing

Cloud forcings were computed as measured or modeled scene-view flux minus clear-sky flux. Because radiosoundings were launched only intermittently and because of the lack of aerosol or ozone measurements, ERA5 clear-sky fluxes were used to calculate all cloud forcings. For computing downward cloud forcing from measured fluxes, ERA5 clear-sky fluxes (hourly) were interpolated to the measurement times (every minute). Classification of measurement-derived downward cloud forcings according to the miniMPL cloud mask, cloud base heights, and cloud base temperatures was conducted after further interpolating cloud forcings onto the miniMPL temporal grid (every 2 min).

ERA5 hourly average downward cloud forcings were classified by lowest-cloud base height using the ERA5 cloud base heights at the mean times for the hourly averages.

The net ERA5 forcings were computed as follows. First, monthly average DLW and DSW forcings, averaged over the study period of 2017–2023, were computed from ERA5 DLW and DSW scene-view and clear-sky fluxes. Next, the same calculation was made for ERA5 upward longwave and shortwave forcings. The upwelling forcings were then subtracted from the downwelling forcings to give the net forcings, following the convention that downward is positive. This was done for longwave, shortwave, and the total (longwave + shortwave) forcing. Corrected ERA5 net forcings were computed in the same manner except that the measured DLW and DSW fluxes were used instead of the ERA5 values. Thus the bias is defined as the difference between ERA5 and the measured all-sky DSW and DLW fluxes for the time period 2017–2023; this bias is applied to correct the ERA5 forcings. The choice to use ERA5 values for clear-sky fluxes, rather than basing them on observations of the atmospheric state, was made due to the paucity of radiosoundings and the lack of other atmospheric measurements (e.g., aerosol or ozone concentrations). Use of ERA5 clear-sky fluxes is supported by the good agreement found between ERA5 and observed temperature and humidity profiles and radiosonde-based DLW clear-sky fluxes (which will be shown). Similarly, the choice to use ERA5 upwelling fluxes was made due to the lack of surface-based upwelling flux measurements. Consequent errors are expected to be small because all-sky and clear-sky upwelling fluxes are similar, such that the upwelling forcings are considerably smaller than the downwelling forcings, as will be shown.

3.5. Identification of ARs

A gridded polar AR scale is calculated from the ERA5 reanalysis data set at $1° \times 1°$ horizontal resolution using the methods introduced by Zhang et al. (2024). The polar AR scale is determined at a specific location based on the duration of AR conditions and the maximum intensity during the AR at each grid point. The AR duration is defined as the period when vertically integrated water vapor transport (IVT) continuously exceeds 100 kg m^{-1} s^{-1}. The AR intensity is defined as the maximum IVT during the AR. After computing the AR duration and intensity, the preliminary polar AR scale is determined based on the AR intensity (In kg m^{-1} s^{-1}, the scale is given as AR-P1: 100–150, AR-P2: 150–200, AR-P3: 200–250, AR1: 250–500, AR2: 500–750, AR3: 750–1,000, AR4: 1,000–1,250, and AR5: >1,250). Last, the final polar AR scale is adjusted from the preliminary scale by promoting by one rank if the AR duration is longer than 48 hr, demoting by one rank if the duration is shorter than 24 hr, or making no change if the duration is 24–48 hr. More details are provided in Section 2.2 in Zhang et al. (2024). In this study, we first select the region of interest (the Northern AP; dashed purple box in Figure 1) and then average the Polar AR scale at each grid point within the box. Only the relatively strong AR

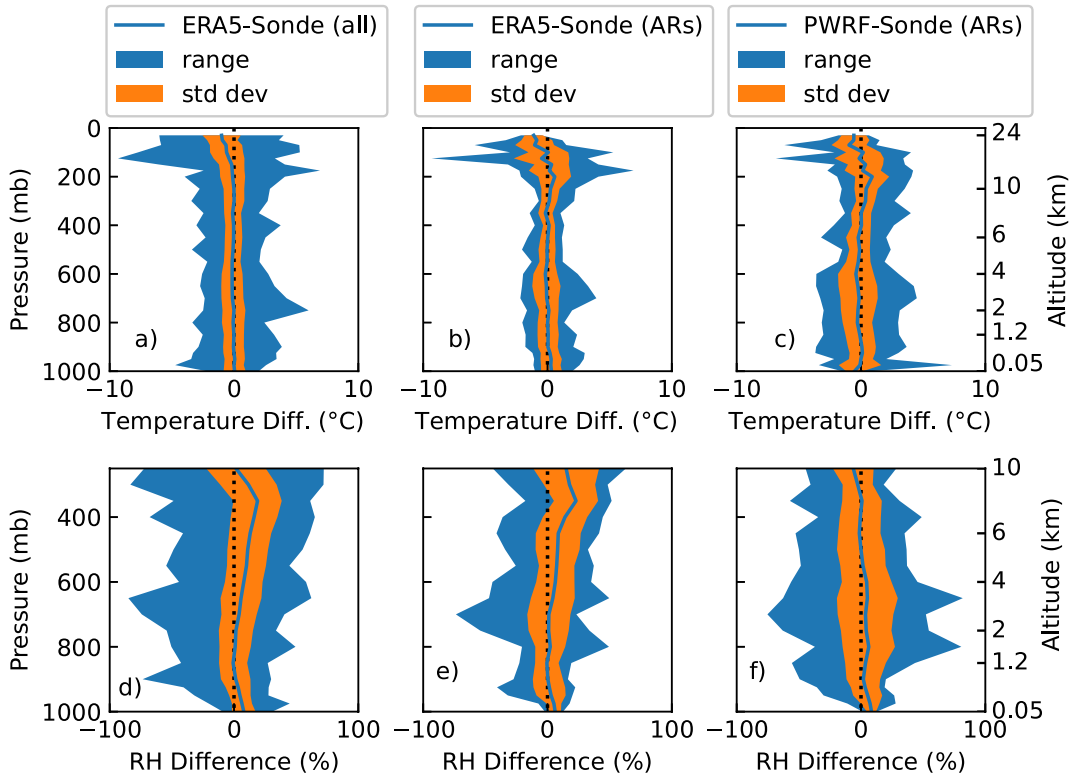

Figure 2. Differences between (a) ERA5 and radiosonde temperature, (b) ERA5 and radiosonde temperature during atmospheric rivers (ARs), (c) PWRF and radiosonde temperature during ARs, (d) ERA5 and radiosonde relative humidity, (e) ERA5 and radiosonde relative humidity during ARs, and (f) PWRF and radiosonde relative humidity during ARs, over Escudero Station on King George Island. Legends at the top correspond to columns. Blue and tan shading gives the range and standard deviation (std dev) of the differences. The right-hand scale gives the average altitudes corresponding to the pressures. Comparisons were made during 2017–2023; comparisons during ARs were for all strong ARs during 2017–2023 in all seasons.

events (AR1 or higher ranks) are included. Events when the AR did not make landfall over the AP were manually filtered out.

4. Results and Discussion

4.1. Atmospheric Temperature and Humidity

Figure 2 shows the differences between radiosonde and model profiles of temperature and relative humidity (model—radiosonde) at Escudero during 2017–2023. The altitude scale shown on the far right is for the average ERA5 profile, since altitudes corresponding to model pressures vary over time. Panels a and d show differences for all radiosoundings, using the ERA5 profiles that are nearest in time and latitude/longitude to Escudero Station. When compared to all radiosondes, ERA5 captures the temperature profiles well, with biases within 0.15°C for pressures above 200 hPa. The ERA5 RH is found to be biased high in the upper troposphere by up to 40%; however given the low absolute humidities in this region, absolute biases are correspondingly low.

Compared to the temperature bias of all cases, the temperature biases during ARs are slightly higher in both ERA5 and PWRF. For ERA5, biases in temperature during ARs are within ±0.4°C for most of the troposphere (altitudes below the 350 hPa pressure level) with positive biases near the surface (altitudes below 900 hPa pressure). For PWRF there are negative biases in the lower troposphere (altitudes below 400 hPa pressure; magnitude of up to 0.6°C) and a small positive bias in the upper troposphere. Standard deviations of the differences are about 1°C, with ranges typically within ±5°C. For ERA5, RH biases during ARs are similar to those for all radiosondes (up to 40%). By contrast, the PWRF RH biases are small: within 9% throughout the first 10 km and peaking in the mid-

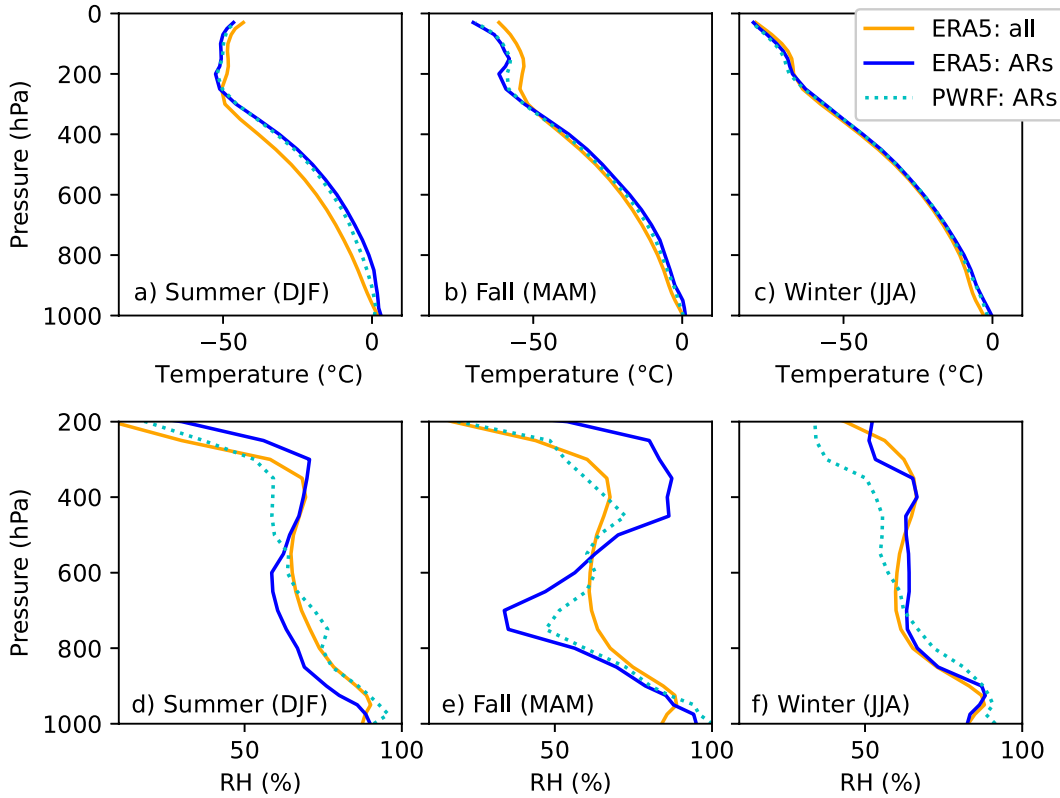

Figure 3. Mean temperature profiles for (a) summer, (b) fall, and (c) winter and mean relative humidity profiles (panels d–f) for the same seasons, respectively. Profiles include means from all ERA5 hourly profiles between 2017 and 2023 (ERA5: all) as well as ERA5 and PWRF hourly profiles during 2017–2023 when strong atmospheric rivers (ARs) were identified (ERA5: ARs and PWRF: ARs) over Escudero Station. The legend in panel c refers to all panels. No ARs were identified during springs within 2017–2023.

troposphere (around 1.2–4 km). This improvement from ERA5 is likely due to the higher resolution of PWRF and may also be influenced by the microphysics scheme tailored for polar regions.

Given that ERA5 temperature profiles agree well with measurements, they are used to compare temperature profiles during AR events to seasonal temperature profiles. These are given in the upper panels of Figure 3 for summer, fall, and winter. Temperatures during AR events are higher throughout the troposphere in all three seasons for both ERA5 and PWRF, as expected given that ARs typically transport warmth from lower latitudes. For RH, we focus on the lower 4 km (pressures above ~600 hPa), where agreement between ERA5 and measurements was best and where most atmospheric water vapor resides. ERA5 relative humidities are found to be lower in the lower troposphere (excluding the near surface) during ARs in the summer and fall compared to the season as a whole, contrary to the expectation of the AR transporting moisture to the AP. This could be because some of the ARs made landfall farther to the south. In addition, there is disagreement between ERA5 and PWRF RH during ARs in the summer and fall. During winter, model results are all fairly similar during ARs and for the season as a whole.

4.2. Cloud Amount

According to ERA5, clouds were present in the grid point closest to Escudero Station 97% of the time during 2017–2023. This is comparable to the estimate from the miniMPl of 96% (P. M. Rowe et al., 2025d). ERA5 cloud amount in summer (DJF) was 97%, in agreement with the miniMPL. However, in other seasons ERA5 indicated a larger fraction of time when clouds existed: 98% compared to ~95% for the miniMPL.

As stated in the methods, to determine the cloud amount for the miniMPL it was assumed that clouds were present when the lidar signal was obscured, which was likely due to fog or precipitation or frost on the enclosure window.

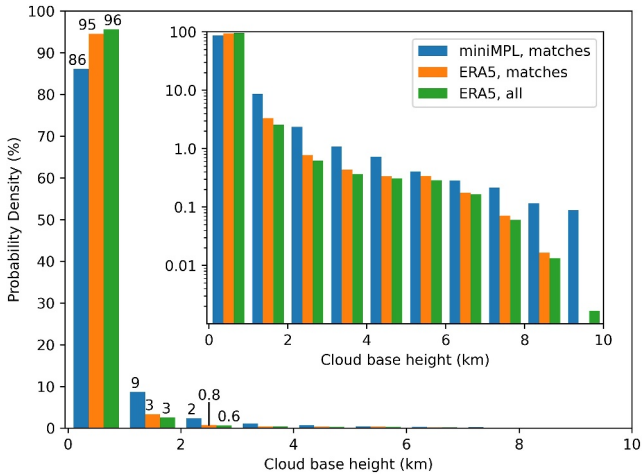

Figure 4. Histograms of hourly cloud base heights from mini micropulse Lidar (miniMPL) measurements made at Escudero Station during 2017–2023. These are compared to hourly ERA5 results near-in-time to miniMPL measurements (ERA5, matches) and to hourly ERA5 results for the entire period (ERA5, all). ERA5 data were taken at the closest grid point to Escudero Station. Bars are labeled with percentages for cloud base heights below 3 km in the main plot. The inset plot shows the same data on a log scale.

In the case of fog or precipitation, a cloud is present. Although frost on the window could occur under clear skies, the high DLW flux during these time periods suggested skies were cloudy (P. M. Rowe et al., 2025d). Obscured cases made up 9.3% of all measurements (9.7% of cloudy-sky measurements). If a portion of these cases were clear it would suggest that the miniMPL cloud amounts were an overestimate, increasing the disparity with ERA5.

4.3. Lowest Cloud Base Height and Temperature

Correlations in lowest cloud base (LCB) heights between ERA5 and measurements made by the miniMPL were found to be weak (correlation coefficient of 0.17 for matched ERA5/miniMPL measurements), with a large root-mean-square difference (1,100 m). The weak correlation could be explained by the differences in field of view between the miniMPL and ERA5. However, as will be discussed in Section 4.4.1 below, sensitivity studies indicate that clouds were often homogeneous over 30 min time periods, and we assume that this observed homogeneity with time is indicative of spatial homogeneity. Thus it seems likely that inaccuracies in ERA5 also contribute to the low correlation observed.

Figure 4 compares the LCB heights derived from the miniMPL to those from ERA5. The blue and orange bins show the probability densities with altitude for the miniMPL and ERA5 at all times between 2017 and 2023 when data were available for both, that is, at hourly intervals when the miniMPL was operational (matches). To create this plot, therefore, miniMPL LCB heights were averaged over hourly intervals. The hourly averaged miniMPL LCB heights agreed with those at a two-minute interval (not shown) to within 1% in each histogram bin. Because only a subset of the period was sampled by the miniMPL, hourly ERA5 LCB heights are also shown for all of 2017–2023 (green). Differences between all ERA5 data and the subsetted data are small compared to differences between the ERA5 data and the measurements. It is evident that the miniMPL observed fewer LCBs in the first 1 km than ERA5 and more clouds at all other altitudes (the inset plot is on a logarithmic scale, making it easier to compare results at higher altitudes). Similar patterns were found for seasonal distributions (not shown).

ERA5 LCBs are found to be at lower heights than those observed with the miniMPL, with 9% more LCB heights within the first 1 km for ERA5. Cloud base heights were not available for 9.7% of cloudy-sky miniMPL measurements, when the atmospheric column was classified as obscured. However, this source of uncertainty can not explain the discrepancy with ERA5. For example, if the LCBs for all obscured cases were above the first 1 km, the percentage for this bin would decrease to 78%, increasing the disparity to 17%. By contrast, If LCBs for all obscured cases were within 1 km it would increase the percentage of observed LCB heights below 1 km to 87%, reducing the disparity by only 1%.

4.4. Broadband Downwelling Radiative Fluxes

4.4.1. Flux Comparisions During Atmospheric Rivers

Figure 5 shows the measured DSW, DLW, and total downwelling radiative flux over Escudero Station during Feb. 2–8, 2019, which included a strong summertime AR event from Feb. 4–6. The measured fluxes are compared to fluxes from ERA5 and PWRF at the closest grid point. The time series is given in the left-hand panels, with the duration of the AR event indicated in white. The left-hand panels also show the clear-sky simulations from ERA5. For DLW, clear-sky simulations created using the radiosonde temperature and humidity profiles are also shown. The flux statistics for the event overall are shown with the box-and-whiskers plots in the right-hand panels.

For this event, PWRF fluxes are found to generally agree well with measurements. ERA5 fluxes, however, are found to be biased toward the clear-sky simulations, with higher DSW values and lower DLW values than the measurements. The good agreement between ERA5 and radiosonde-measurement-based clear-sky simulations suggests that this is not due to errors in the calculation of the atmospheric state in ERA5.

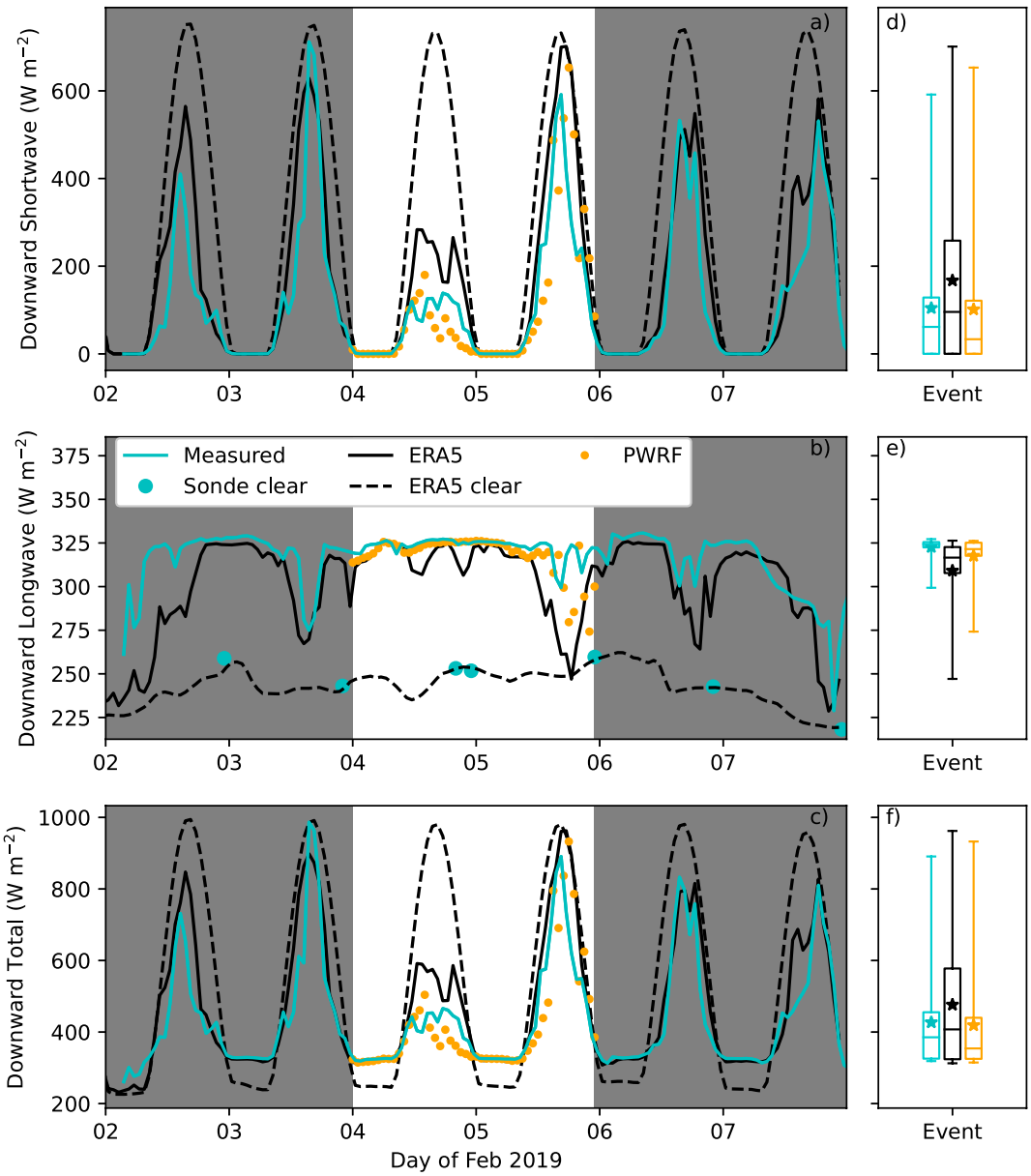

Figure 5. Downwelling radiative flux at the surface during an atmospheric river in summer over Escudero Station on King George Island. Panels (a–c) show time series of downwelling broadband radiation for ERA5 clear-sky simulations (ERA5 clear), ERA5 and PWRF fluxes for the scene view, and fluxes from measurements on King George Island, after averaging over an hour. The white regions of panels (a–c) indicate the timespan of the AR event. Panels (d–f) show box-and-whiskers plots for the event. The colors correspond to the legend. The mean is indicated by an asterisk, the median by a horizontal bar, the interquartile range by boxes, and the full range by whiskers.

Tables 2 and 3, introduced previously, show the mean biases in ERA5 and PWRF compared to measurements for each AR event. In summer (Table 2), for all but one strong AR case the ERA5 DSW is found to be biased high, and all ERA5 DLW values are found to be biased low: Mean biases for the summer AR events are found to be 31 W m^{-2} for DSW and −16 W m^{-2} for DLW. PWRF biases have overall smaller magnitudes, with mean flux biases during strong summer ARs of −12 W m^{-2} for DSW and −2 W m^{-2} for DLW. As was discussed in regards to RH, the more-accurate fluxes computed by PWRF relative to ERA5 are likely linked to PWRF's finer spatial resolution and polar-specific microphysics scheme.

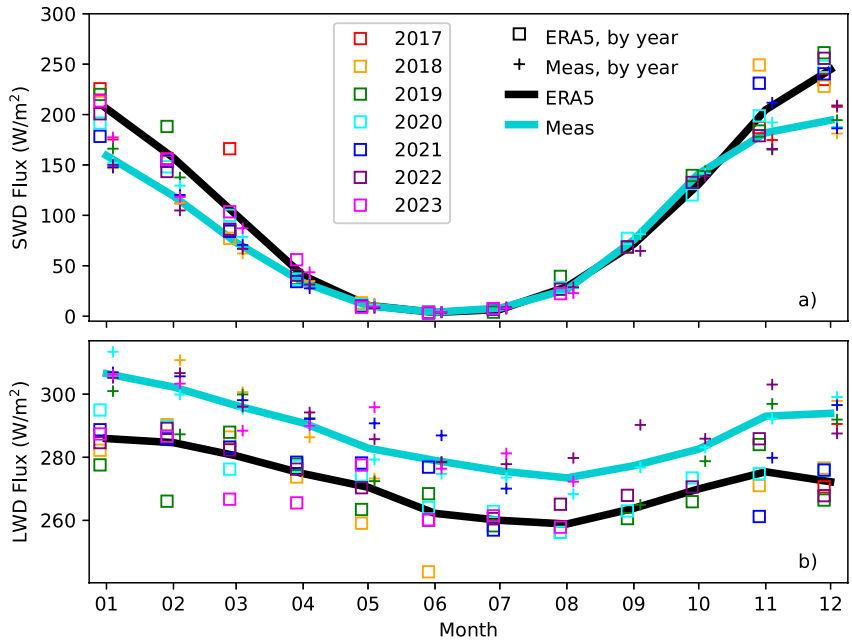

Figure 6. (a) Monthly averages of hourly average shortwave downwelling radiative flux (DSW Flux) and (b) monthly averages of hourly average longwave downwelling radiative flux (DLW Flux) measured at the surface at Escudero Station, compared to ERA5 reanalysis results at the closest grid point. Solid lines give weighted means of available data over 2017–2023. Symbols, which represent annual values (see legend), are offset slightly along the *x*-axis for visibility. The legend in panel (a) also corresponds to (b).

During strong fall and winter ARs (Table 3), the mean DLW biases are negative for ERA5 and PWRF, as for summer. The mean DLW bias found for ERA5 is similar to the summertime bias, whereas for PWRF the bias is roughly three times as large. The fall and winter DSW biases are small in magnitude due to the low solar insolation.

An important caveat to these results regards the difference in field of view corresponding to the fluxes, given that ERA5 and PWRF are for large regions mainly consisting of open ocean, whereas the measurements are made of the sky hemisphere from a single point on the island. To test the importance of differences in field of view, P. M. Rowe et al. (2025d) examined the sky cloudiness and cloud phase heterogeneity by examining how much the miniMPL lidar column classification for this data set varied in time, using the time variation as a proxy for spatial variation. It was found that over a 30-min period 84%–98% of Lidar cloud measurements passed the criterion that the column measurement type match the most commonly observed column measurement type within the time window. This suggests that the sky cloudiness was often stable, indicating that the time-averaging done in this work before comparing measurements to ERA5 will aid comparability. Please see P. M. Rowe et al. (2025d) for more detail. Comparing PWRF and ERA5 model results for a larger area is an important topic of future work.

It is important to note that for DSW fluxes the magnitude of the biases is strongly influenced by the solar angles during the strong AR events, which in turn depend on the latitude and time of year.

4.4.2. Flux Comparisons Over the Seasonal Cycle

Hourly averages of DSW and DLW fluxes measured at Escudero Station are found to be correlated with ERA5 results with a correlation coefficient of 0.72.

Figure 6 compares monthly average DSW and DLW fluxes measured at the surface at Escudero Station to ERA5 results for the closest grid point. Biases in ERA5 monthly average summertime DSW fluxes are 38–50 W m^{-2} (By comparison, the average bias during summertime ARs was found to be 30.9 W m^{-2}, but given the large variation among DSW biases during strong ARs, of −52.9 to 76.7 W m^{-2}, more data are needed to determine if this difference is significant.) Moreover, DSW flux biases have a strong seasonal cycle, with biases near zero in June, when the sun is below the horizon for most of the day.

ERA5 monthly DLW flux averages are found to be biased low by 18–22 W m^{-2} in summer, with a weak seasonal cycle and an average bias of −16 W m^{-2} over the year. This is similar to results obtained by Cerovecki et al. (2022) who found a bias of −20 W m^{-2} at 54.08°S, 89.67°W, and to the biases of −14.1 and −19.3 W m^{-2} found by Silber et al. (2019) at McMurdo station and the West Antarctic Ice Sheet, respectively.

Because the broadband instruments occasionally experienced down time, the ERA5 data during 2017–2023 was also compared to ERA5 data at measurement times to ensure that the measurement temporal coverage was sufficient to accurately represent the monthly averages. This comparison (not shown) indicated that the subset of data at measurement times did a good job representing the entire time series, with DLW and DSW flux differences between ERA5 monthly means for all times compared to the subset at measurement times within ±2 W m^{-2} (See P. M. Rowe et al., 2025d for the number of points that were used in the comparison for each month and year.).

Underestimating DLW flux could be explained by clouds that are not warm enough, either due to biased-low model temperatures or biased-high model cloud bases. However, the slight negative biases in ERA5 temperature found between 10 and 24 km (referring back to Figure 2) are too small and too high in the atmosphere to account for the negative biases seen in the ERA5 DLW fluxes compared to the measurements, which would require temperature biases of around −4°C for optically thick low clouds. Biased-low cloud bases can also be ruled out since, as discussed previously, compared to observations ERA5 predicts more LCBs below 1 km, where the atmosphere is typically warmer. This would lead to DLW fluxes that are generally stronger relative to the observations, opposite to the trend observed. Another explanation for too-low DLW fluxes could be biases due to ignoring the temperature dependence of the complex refractive indices of supercooled liquid water in the models (P. M. Rowe et al., 2020); however, this effect is expected to be small given that the liquid cloud is typically close to 0°C (P. M. Rowe et al., 2013). Moreover, in addition to the underestimation of DLW flux, the explanation also needs to account for the overestimation of DSW flux.

Model biases that lead to both overestimating DSW and underestimating DLW include model atmospheres that are too dry, insufficiently cloudy, or lacking in supercooled liquid water relative to ice. These are in keeping with the results of Silber et al. (2019), who found that both Antarctic WRF Mesoscale Prediction System (of the national science foundation national center for atmospheric research) and ERA5 underestimated the surface DLW radiation at McMurdo Station and the West Antarctic Ice Sheet Divide, which they attribute to insufficient humidity, underestimated liquid cloud, and overestimated ice cloud. However, over Escudero ERA5 was found to have slightly biased-high (rather than biased-low) relative humidity (referring back to Figure 2). Insufficient cloudiness could be due to too little cloud or cloud that is too thin. Given that there was agreement in the amount of time the sky was cloudy according to ERA5 and the miniMPL observations in summer, as discussed earlier, the most likely remaining possibilities are that ERA5 modeled clouds that are too optically thin or underestimated liquid relative to ice. To explore these possibilities, we next examine the cloud forcing.

4.5. Cloud Forcing

4.5.1. Biases in ERA5

To explore whether the biases found in ERA5 are likely due to insufficient overall cloudiness or insufficient liquid relative to ice, Figure 7 shows histograms of DLW forcing for observations and for ERA5. The top two panels show the distributions separately for observed fluxes when the miniMPL classified the atmospheric column as liquid-containing or ice-only, whereas the bottom panel shows the distribution for all time periods identified as cloudy by ERA5. Colors indicate the temperature at the cloud base as determined by the miniMPL (top two panels) and by ERA5 (bottom panel). Because Figure 7 excludes a large fraction of the measured forcings in order to enable categorizing by LCB height, before discussing the figure it is important to ensure that the subsetted data are fairly representative of all cloudy times.

To determine the effect of subsetting the measured forcings, distributions for all measured forcings (2,359,657 points) were compared to measured forcings matched to the times of miniMPL measurements (611,838 points). This is an important check because although the pyrgeometer ran nearly continuously, the miniMPL mainly ran during warmer months. Distributions were visually similar (not shown) and means (67.0 and 67.8 W m^{-2}) and medians (77.0 and 77.4 W m^{-2}) were found to agree within 1 W m^{-2}, with slightly higher values when the miniMPL was running. This indicates that using only times when the miniMPL was operating, which effectively weights the results toward the warmer months, had only a small effect on the distributions. Similarly, because

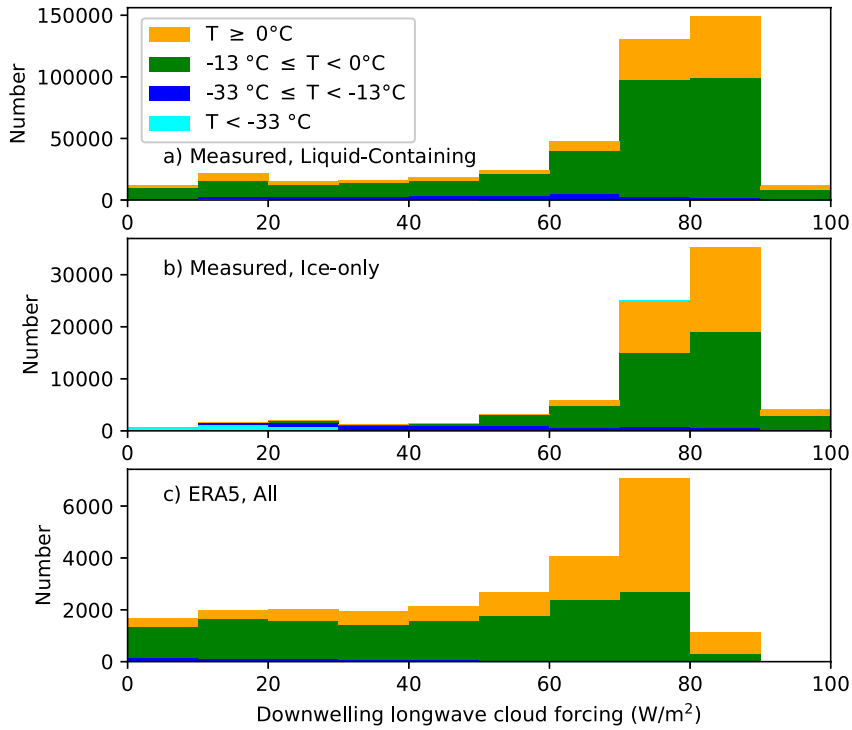

Figure 7. Observed downwelling longwave cloud forcing distributions over 2017–2023 at Escudero Station, King George Island, when (a) liquid-containing clouds were present and (b) ice-only clouds were present, compared to (c) downwelling longwave distributions from ERA5 for the same time range, at the closest grid point. Colors indicate the temperature of the cloud base of the lowest cloud layer; the legend in the top panel refers to all panels.

ERA5 forcings shown in Figure 7 are for all time periods identified as cloudy by ERA5, it is important to compare this set of forcings to the subset when the miniMPL was operational. In contrast to the measured forcings, the mean for all ERA5 cloudy-sky forcings (51.7 W m^{-2}) is found to be higher than that when the miniMPL was operational (49.1 W m^{-2}), with similar results for the medians (59.4 and 56.2 W m^{-2}). This suggests that including all cloudy time periods would increase the discrepancy between measured and ERA5 forcings slightly, but not have a large effect.

It is also important to determine the effect of excluding measured forcings when the cloud phase was unknown (0.8% of cloudy observations) or where the cloud base height could not be determined because the Lidar was obscured (9.7% of cloudy observations). Because forcings were overall higher when the column was classified as obscured (P. M. Rowe et al., 2025d) the distributions shown are shifted toward slightly lower values compared to all cloudy cases: for combined measured liquid-containing and ice-only observations, the mean flux is 68.5 W m^{-2} for the cases shown in Figure 7 compared to a mean of 69.8 W m^{-2} for all cloudy cases. Medians are 77.0 and 77.9 W m^{-2}, respectively. However, these differences of less than 1 W m^{-2} due to subsetting are small compared to the differences of around 15 W m^{-2} when comparing means for ERA5 and measured cloud forcings. Therefore conclusions drawn from comparing the subsetted differences categorized by cloud base height can be assumed to hold well for all cases.

Returning to the discussion of Figure 7, distributions for observed ice-only clouds are found to be fairly similar overall to those for liquid-containing clouds, but markedly different from the ERA5 distributions. (Note that although there are some ice-only clouds above 0°C, these were below 3°C and are likely due to small inaccuracies in temperature). The peaks in the ERA5 distributions for clouds with cloud base temperatures above −13°C (LCB heights below 400 m and from 400 to 2,000 m, as shown in Figure S1 of Supporting Information S1) are both shifted toward lower forcings by 10 W m^{-2}, with a significantly higher fraction of clouds in the low end of the tail, consistent with optically thinner clouds. For cloud base temperatures above −13°C, means are 68 and 79 W m^{-2} for observed liquid-containing and ice-only columns compared to 53 W m^{-2} for ERA5. Similarly, for clouds with LCB temperatures between −33°C and −13°C, means are 53 and 48 W m^{-2} for observed liquid-containing and

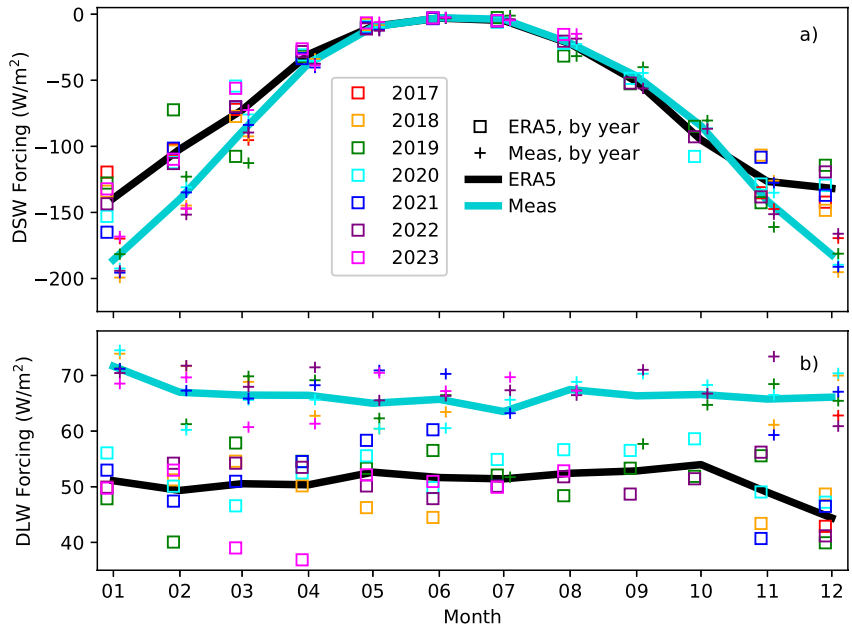

Figure 8. (a) Monthly averages of hourly average shortwave downwelling cloud forcing (DSW Forcing) and (b) monthly averages of hourly average longwave downwelling cloud forcing (DLW Forcing) measured at the surface at Escudero Station, compared to ERA5 reanalysis results at the closest grid point. Solid lines give weighted means of available data over 2017–2023. Symbols, which represent annual values (see legend), are offset slightly for visibility. The legend in panel (a) also corresponds to (b).

ice-only columns, compared to 24 W m^{-2} for ERA5. When separated by cloud phase, distributions for ERA5 vary slightly but mean values are similar for liquid-containing and ice-only atmospheric columns, as shown in Figure S2 of Supporting Information S1. Overall, ERA5 models slightly more total cloud liquid water than ice water for the dates analyzed here (which are biased toward summertime) with average values of 57 and 36 g m^{-2} respectively. Most ERA5 clouds include both liquid and ice.

For clouds with LCB temperatures below −13°C all three distributions differ, with LCB temperature medians of 53, 35, and 19 W m^{-2} for liquid-containing observations, ice-only observations, and ERA5 clouds, respectively. Indeed, it is only for these colder, higher clouds that ice-only cloud forcing distributions are significantly lower than for liquid-containing clouds (as pointed out in P. M. Rowe et al., 2025d), and for these cases the ERA5 data resembles the ice-only observations more than the liquid-containing observations.

Taken together, this suggests that it is only for LCB temperatures below about −13°C that the differences between measured and ERA5 forcings could be explained by insufficient supercooled liquid in clouds, consistent with the findings of Silber et al. (2019). However, given the small fraction of clouds with LCB temperatures below −33°C, this could explain only a small portion of the ERA5 DLW forcing biases. Instead, the observed cloud forcings for clouds with LCB temperatures above −33°C (LCB heights typically below 2,000 m), which make up 94% of the lowest clouds, suggest that low ice clouds are *not* optically thinner than liquid-containing clouds. Given that ice particles are generally much larger than their liquid counterparts, this also suggests that cloud particle size is not the explanation. Instead, the most likely explanation for ERA5 underestimating DLW forcings is due to modeling clouds that are optically too thin due to insufficient cloud water content. Future work is needed to qualitatively assess these possibilities, including detailed radiative transfer equations that demonstrate the sensitivity of ERA5 cloud fluxes to increased optical depth, as well as the importance of the atmosphere below the clouds. Additional measurements of cloud properties are also crucial to allow for detailed comparison of cloud properties.

4.5.2. Monthly Average Cloud Forcing

Monthly average downward cloud forcings are shown in Figure 8. The observed DSW monthly mean forcings range from a minimum of −200 W m^{-2} in January to a maximum of −2.4 W m^{-2} in June. By contrast, most mean

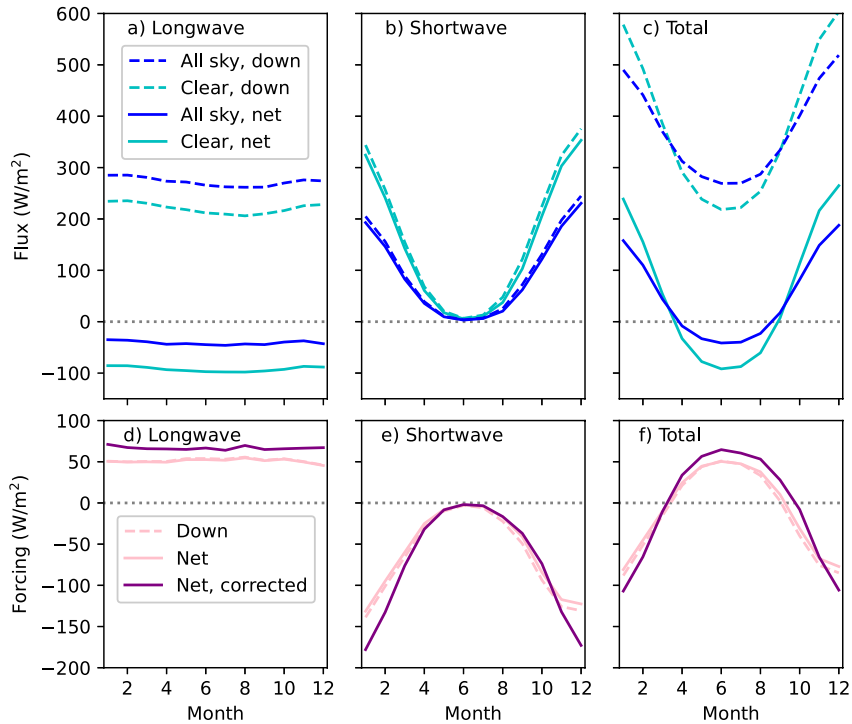

Figure 9. Monthly average ERA5 fluxes and cloud forcing components for 2017–2023 at the grid point nearest Escudero Station. The net forcings given in panels (d–f) were corrected (Net, corrected) for the bias found between ERA5 and measured downwelling fluxes.

monthly observed DLW forcings fall into a much smaller range, between 60 and 75 W m^{-2}. DSW forcings dominate in summer, whereas DLW forcings dominate in winter, with transitions in fall and spring.

Because forcings computed from both ERA5 products and observed downwelling fluxes were calculated by subtracting ERA5 clear sky downwelling fluxes, biases in forcings are the same as biases in downward radiative fluxes. Thus both ERA5 DSW fluxes and forcings are consistently higher than observations in summer, whereas ERA5 DLW fluxes and forcings are biased low throughout the year.

These results are consistent with the findings of Wang et al. (2020), who also found positive biases in ERA5 downwelling shortwave radiation and negative biases in the DLW compared to ship-based observations over the SO between coastal East Antarctica and Hobart, Australia (within 42.8°S to 78.7°S and 62.6°E to 157.7°W).

4.5.3. Implications for the Southern Ocean

So far, we have focused on downwelling fluxes and cloud forcings. However, the surface energy balance depends on the net (downwelling—upwelling) cloud forcing. Figure 9 compares the DLW cloud flux and forcing components to the net values for ERA5 results at the grid point nearest Escudero, for monthly averages over 2017–2023. Because the longwave surface albedo is low, net longwave cloud forcing is nearly the same as the DLW cloud forcing (overlapping pink solid and dashed lines in panel d). For the shortwave, by contrast, the surface albedo can be highly variable. For example, over open ocean surface albedos are low (~0.06) and the net shortwave forcings are also only slightly weaker than the DSW forcings (pink solid and dashed lines in panel e, for which shortwave albedo varies from 0.06 in January to 0.18 in June). Thus our results for downward forcings can be taken to be similar to expected net forcings over bare land and open ocean at the latitude of Escudero Station. Over the SO at this latitude, therefore, in the summer net shortwave forcing is expected to dominate over net longwave forcing, causing clouds to have an overall cooling effect, whereas in winter clouds have an overall net warming effect (pink curves in panel f).

In contrast to open ocean, over snow and ice significant radiation is reflected by the surface, and the net SW cloud forcing may be reduced by 50%–80%. For example, for a SW downward forcing of −170 W m^{-2} (the summertime

mean), the SW net forcing over snow and ice would be around −30 to −85 W m^{-2}, which is comparable to the LW net forcing of ∼68 W m^{-2}. Importantly, this means that over snow-covered land or over sea ice, clouds can have a net radiative warming effect, even in summer.

Panels d–f also give the net forcing after correcting for the bias found in the ERA5 downwelling fluxes through comparison to measurements, as described in the methods. After correcting for the bias, the monthly average net cloud forcing is found to be a minimum of −107 W m^{-2} in January and a maximum of 65 W m^{-2} in June. Clouds over the SO near Escudero Station are found to cause an overall cooling effect in summer and a warming effect during fall, winter, and spring (early March–early September). Moreover, ERA5 is found to underpredict the time span when clouds cause an overall warming, during September, by about 16 days.

5. Conclusions

Comparisons between ERA5 and observations made on King George Island indicate that ERA5 continues to overestimate DSW radiation reaching the SO and underestimate DLW radiation. Monthly average ERA5 DSW radiative fluxes averaged over 2017–2023 are found to be 38–50 W m^{-2} higher than observations in the summer, whereas monthly average ERA5 DLW fluxes are found to vary between 18 and 22 W m^{-2} lower than observations over the annual cycle. During strong AR events, flux biases for ERA5 are found to be similar, whereas, by contrast, PWRF downwelling flux biases are found to be much smaller (averages of −12 W m^{-2} for DSW and −2 W m^{-2} for DLW).

Despite the low biases found in ERA5 DLW fluxes, ERA5 is found to have slightly higher cloud amounts than observed at Escudero Station, with a greater proportion of clouds in the lowest 400 m of the atmosphere, where temperatures are typically warmer than at higher altitudes. Moreover, temperature and humidity profiles agree fairly well with in situ radiosonde measurements. With cloud properties otherwise the same, having a greater proportion of warmer, lower clouds in ERA5 would result in more DLW radiation, opposite to the trend observed here of biased-low ERA5 DLW radiation. The discrepancy with observed DLW radiation therefore seems likely to be due to differences in cloud optical depth. These differences could be explained by a biased-high proportion of ice relative to liquid. However, the DLW forcing distributions for ice clouds were found to be similar to those for liquid-containing clouds, indicating that the DLW forcing is not very sensitive to cloud phase. Therefore, although quantitative measurements are needed, we speculate that biases in ERA5 DLW in this region are primarily due to inaccurate cloud water content in low-level clouds, with insufficient supercooled liquid water above 1,000 m making at most a small contribution to ERA5 DSW biases.

After correcting ERA5 cloud forcings for the bias determined through comparison to measurements, the monthly average net cloud forcing over 2017–2023 exhibits a minimum of −107 W m^{-2} in January and a maximum of 65 W m^{-2} in June.

This comparison of measurements to ERA5 is unique in its duration and location. King George Island is located near the northern edge of the Antarctic sea ice zone, where downward longwave radiative flux impacts sea ice expansion (Cerovecki et al., 2022) but where surface-based measurements are lacking. Because of the influence of the circumpolar westerly winds, King George Island is broadly representative of this high-latitude region of the Southern Ocean. Overall, our results point to a need for additional measurements in this location, particularly in situ measurements within clouds, to better characterize cloud liquid, ice water content, and optical thickness. Such measurements are crucial for improving our understanding of how clouds and their interactions with radiation differ during atmospheric rivers and for quantifying biases in reanalysis data and model simulations such as those in ERA5, including those used for future projections under climate change.

Data Availability Statement

The data used in this manuscript are available as follows: Escudero cloud mask data derived from the micropulse lidar: Stillwell et al. (2025); Escudero radio sounding data: P. Rowe et al. (2025b); Escudero downward longwave radiative fluxes: P. Rowe et al. (2025a); and Escudero shortwave radiative fluxes: P. Rowe et al. (2025c). Models and model data are available as follows: ERA5 reanalysis data: Copernicus Climate Change Service (2023); the PWRF model: Bromwich et al. (2023); and the Reference Elevation Model of Antarctica (REMA) topography

used in PWRF: Gerber and Lehning (2020). Software used for analysis and figure creation is available at P. Rowe (2025). Figures were created with matplotlib in Python.

Acknowledgments
Research at Escudero Station was supported by the Instituto Antártico Chileno (INACH). We thank N. Dettling, J. Jorquera, F. Cabello, J. Carrera, and B. Valdevenito for maintaining the instrument platform and collecting data. Material derived from analysis of the micropulse lidar data are based upon the work supported by the NSF National Center for Atmospheric Research, which is a major facility sponsored by the National Science Foundation under Cooperative Agreement No. 1852977. We are grateful to three anonymous reviewers who provided useful suggestions to this paper. This work was funded by National Science Foundation Grants 2127632, 2229392, and 2205398. RRC acknowledges the support of INACH (RT_69-20), ANID (FONDECYT 1231904), and USACH-DICYT 092431CC_Ayudante. IG acknowledges support from Portuguese FCT for strategic funding to CIIMAR (UIDB/04423/2020, UIDP/04423/2020), CEEC IND IMPACT (2021.03140. CEECIND/CP1659/CT0005), and Portuguese Polar Program.

References

Alkama, R., Taylor, P. C., Garcia-San Martin, L., Douville, H., Duveiller, G., Forzieri, G., et al. (2020). Clouds damp the radiative impacts of polar sea ice loss. *The Cryosphere*, *14*(8), 2673–2686. https://doi.org/10.5194/tc-14-2673-2020

Bodas-Salcedo, A., Williams, K. D., Field, P. R., & Lock, A. P. (2012). The surface downwelling solar radiation surplus over the Southern Ocean in the Met Office model: The role of midlatitude cyclone clouds. *Journal of Climate*, *25*(21), 7467–7486. https://doi.org/10.1175/jcli-d-11-00702.1

Bodas-Salcedo, A., Williams, K. D., Ringer, M. A., Beau, I., Cole, J. N., Dufresne, J. L., et al. (2014). Origins of the solar radiation biases over the Southern Ocean in CFMIP2 models. *Journal of Climate*, *27*(1), 41–56. https://doi.org/10.1175/jcli-d-13-00169.1

Bromwich, D. H., Hines, K. M., & Bai, L.-S. (2023). Polar WRF version 4.5.1 [Software]. https://polarmet.osu.edu/PWRF/

Bromwich, D. H., Otieno, F. O., Hines, K. M., Manning, K. W., & Shilo, E. (2013). Comprehensive evaluation of polar weather research and forecasting model performance in the Antarctic. *Journal of Geophysical Research: Atmospheres*, *118*(2), 274–292. https://doi.org/10.1029/2012jd018139

Bromwich, D. H., Werner, K., Casati, B., Powers, J. G., Gorodetskaya, I. V., Massonnet, F., et al. (2020). The Year Of Polar Prediction in the Southern Hemisphere (YOPP-SH). *Bulletin of the American Meteorological Society*, *101*(10), E1653–E1676. https://doi.org/10.1175/bams-d-19-0255.1

Ceppi, P., Hwang, Y. T., Frierson, D. M., & Hartmann, D. L. (2012). Southern Hemisphere jet latitude biases in CMIP5 models linked to shortwave cloud forcing. *Geophysical Research Letters*, *39*(19). https://doi.org/10.1029/2012gl053115

Cerovecki, I., Sun, R., Bromwich, D. H., Zou, X., Mazloff, M. R., & Wang, S.-H. (2022). Impact of downward longwave radiative deficits on Antarctic sea-ice extent predictability during the sea ice growth period. *Environmental Research Letters*, *17*(8), 084008. https://doi.org/10.1088/1748-9326/ac7d66

Chyhareva, A., Gorodetskaya, I., Krakovska, S., Pishniak, D., & Rowe, P. (2021). Precipitation phase transition in austral summer over the Antarctic Peninsula. *Ukrainian Antarctic Journal*, (1), 32–46. https://doi.org/10.33275/1727-7485.1.2021.664

Copernicus Climate Change Service. (2023). ERA5 hourly data on pressure levels from 1940 to present. *Copernicus Climate Change Service (C3S) Climate Data Store (CDS)*. https://doi.org/10.24381/cds.bd0915c6

Corbea-Pérez, A., Calleja, J. F., Recondo, C., & Fernández, S. (2021). Evaluation of the MODIS (C6) daily albedo products for Livingston Island, Antarctic. *Remote Sensing*, *13*(12), 2357. https://doi.org/10.3390/rs13122357

Cox, C. J., Walden, V. P., Rowe, P. M., & Shupe, M. D. (2015). Humidity trends imply increased sensitivity to clouds in a warming Arctic. *Nature Communications*, *6*(1), 10117. https://doi.org/10.1038/ncomms10117

Deb, P., A. Orr, A., Hosking, J. S., Phillips, T., Turner, J., Bannister, D., et al. (2016). An assessment of the Polar Weather Research and Forecasting (WRF) model representation of near-surface meteorological variables over West Antarctica. *Journal of Geophysical Research: Atmospheres*, *121*(4), 1532–1548. https://doi.org/10.1002/2015JD024037

Gerber, F., & Lehning, M. (2020). REMA topography and AntarcticaLC2000 for WRF [Dataset]. *EnviDat*. https://doi.org/10.16904/envidat.190

Gilbert, E., Orr, A., King, J. C., Renfrew, I. A., Lachlan-Cope, T., Field, P. F., & Boutle, I. A. (2020). Summertime cloud phase strongly influences surface melting on the Larsen C ice shelf, Antarctica. *Quarterly Journal of the Royal Meteorological Society*, *146*(729), 1575–1589. https://doi.org/10.1002/qj.3753

Gorodetskaya, I. V., Durán-Alarcón, C., González-Herrero, S., Clem, K. R., Zou, X., Rowe, P., et al. (2023). Record-high Antarctic Peninsula temperatures and surface melt in February 2022: A compound event with an intense atmospheric river. *npj climate and atmospheric science*, *6*(1), 202. https://doi.org/10.1038/s41612-023-00529-6

Hersbach, H., Bell, B., Berrisford, P., Hirahara, S., Horanyi, A., Muñoz-Sabater, J., et al. (2020). The ERA5 global reanalysis. *Quarterly Journal of the Royal Meteorological Society*, *146*(730), 1999–2049. https://doi.org/10.1002/qj.3803

Himmich, K., Vancoppenolle, M., Madec, G., Sallée, J. B., Holland, P. R., & Lebrun, M. (2023). Drivers of Antarctic sea ice advance. *Nature Communications*, *14*(1), 6219. https://doi.org/10.1038/s41467-023-41962-8

Hines, K. M., Bromwich, D. H., Bai, L., Bitz, C. M., Powers, J. G., & Manning, K. W. (2015). Sea ice enhancements to Polar WRF. *Monthly Weather Review*, *143*(6), 2363–2385. https://doi.org/10.1175/MWR-D-14-00344.1

Hines, K. M., Bromwich, D. H., Silber, I., Russell, L. M., & Bai, L. (2021). Predicting frigid mixed-phase clouds for pristine coastal Antarctica. *Journal of Geophysical Research: Atmospheres*, *126*(23), e2021JD035112. https://doi.org/10.1029/2021jd035112

Hines, K. M., Wang, I. S., Verlinde, J., & Lubin, D. (2019). Microphysics of summer clouds in central West Antarctica simulated by the polar Weather Research and Forecasting Model (WRF) and the Antarctic Mesoscale Prediction System (AMPS). *Atmospheric Chemistry and Physics*, *19*, 12431–12454. https://doi.org/10.5194/acp-19-12431-2019

Howat, I. M., Porter, C., Smith, B. E., Noh, M.-J., & Morin, P. (2019). The reference elevation model of Antarctica. *The Cryosphere*, *13*(2), 665–674. https://doi.org/10.5194/tc-13-665-2019

Hu, Y., Rodier, S., Xu, K. M., Sun, W., Huang, J., Lin, B., et al. (2010). Occurrence, liquid water content, and fraction of supercooled water clouds from combined CALIOP/IIR/MODIS measurements. *Journal of Geophysical Research*, *115*(19), 937. https://doi.org/10.1029/2009JD012384

Huang, Y., Siems, S. T., Manton, M. J., Protat, A., & Delanoë, J. (2012). A study on the low-altitude clouds over the Southern Ocean using the DARDAR-MASK. *Journal of Geophysical Research*, *117*(17). https://doi.org/10.1029/2012JD017800

Hwang, Y. T., & Frierson, D. M. (2013). Link between the double-intertropical convergence zone problem and cloud biases over the Southern Ocean. *Proceedings of the National Academy of Sciences* (Vol. 110(13), pp. 4935–4940). https://doi.org/10.1073/pnas.1213302110

Hyder, P., Edwards, J. M., Allan, R. P., Hewitt, H. T., Bracegirdle, T. J., Gregory, J. M., et al. (2018). Critical Southern Ocean climate model biases traced to atmospheric model cloud errors. *Nature Communications*, *9*(1), 3625. https://doi.org/10.1038/s41467-018-05634-2

Kay, J. E., Wall, C., Yettella, V., Medeiros, B., Hannay, C., Caldwell, P., & Bitz, C. (2016). Global climate impacts of fixing the Southern Ocean shortwave radiation bias in the Community Earth System Model (CESM). *Journal of Climate*, *29*(12), 4617–4636. https://doi.org/10.1175/jcli-d-15-0358.1

Liang, Y., Bi, H., Huang, H., Lei, R., Liang, X., Cheng, B., & Wang, Y. (2022). Contribution of warm and moist atmospheric flow to a record minimum July sea ice extent of the Arctic in 2020. *The Cryosphere*, *16*(3), 1107–1123. https://doi.org/10.5194/tc-16-1107-2022

Lubin, D., Zhang, D., Silber, I., Scott, R. C., Kalogeras, P., Battaglia, A., et al. (2020). AWARE in west Antarctica. *Bulletin of the American Meteorological Society*, *101*(10), 892–898. https://doi.org/10.1175/bams-d-18-0278.a

Mace, G. G., Zhang, Q., Vaughan, M., Marchand, R., Stephens, G., Trepte, C., & Winker, D. (2009). A description of hydrometeor layer occurrence statistics derived from the first year of merged Cloudsat and CALIPSO data. *Journal of Geophysical Research*, *114*(D8). https://doi.org/10.1029/2007jd009755

Mason, S., Jakob, C., Protat, A., & Delanoë, J. (2014). Characterizing observed midtopped cloud regimes associated with Southern Ocean shortwave radiation biases. *Journal of Climate*, *27*(16), 6189–6203. https://doi.org/10.1175/jcli-d-14-00139.1

McFarquhar, G. M., Bretherton, C. S., Marchand, R., Protat, A., DeMott, P. J., Alexander, S. P., et al. (2021). Observations of clouds, aerosols, precipitation, and surface radiation over the Southern Ocean: An overview of CAPRICORN, MARCUS, MICRE, and SOCRATES. *Bulletin of the American Meteorological Society*, *102*(4), E894–E928. https://doi.org/10.1175/bams-d-20-0132.1

Morrison, H., & Milbrandt, J. A. (2015). Parameterization of cloud microphysics based on the prediction of bulk ice particle properties. Part I: Scheme description and idealized tests. *Journal of the Atmospheric Sciences*, *72*(1), 287–311. https://doi.org/10.1175/JAS-D-14-0065.1

Naud, C. M., Booth, J. F., & Del Genio, A. D. (2014). Evaluation of ERA-interim and MERRA cloudiness in the Southern Ocean. *Journal of Climate*, *27*(5), 2109–2124. https://doi.org/10.1175/jcli-d-13-00432.1

Rowe, P. (2025). prowe12/Antarctic-Peninsula: Comparison of atmospheric observations over Escudero to models: April 11, 2025 release (version 2.0.0) [Software]. *Zenodo*. https://doi.org/10.5281/zenodo.15199823

Rowe, P., Cordero, R., Zou, X., & Gorodetskaya, I. (2025a). Longwave downward radiative flux (king George Island), 2017 - 2023 [Dataset]. *AMRDC Data Repository*. https://doi.org/10.48567/hnhz-f486

Rowe, P., Cordero, R., Zou, X., & Gorodetskaya, I. (2025b). Radiosonde measurements (King George Island), 2017 - 2023 [Dataset]. *AMRDC Data Repository*. https://doi.org/10.48567/jqv8-r657

Rowe, P., Cordero, R., Zou, X., & Gorodetskaya, I. (2025c). Shortwave downward radiative flux (King George Island), 2017–2023 [Dataset]. https://doi.org/10.48567/peeg-7j35

Rowe, P. M., Fergoda, M., & Neshyba, S. (2020). Temperature-dependent optical properties of liquid water from 240 to 298 K. *Journal of Geophysical Research: Atmospheres*, *125*(17), e2020JD032624. https://doi.org/10.1029/2020jd032624

Rowe, P. M., Neshyba, S., & Walden, V. P. (2013). Radiative consequences of low-temperature infrared refractive indices for supercooled water clouds. *Atmospheric Chemistry and Physics*, *13*(23), 11925–11933. https://doi.org/10.5194/acp-13-11925-2013

Rowe, P. M., Zou, X., Gorodetskaya, I., Stillwell, R., Cordero, R. R., Sepulveda, E., et al. (2025d). Observations of clouds and radiation over King George Island and implications for the Southern Ocean and Antarctica. *In Review for Journal of Geophysical Research: Atmospheres*. https://doi.org/10.1029/2024JD042787

Sato, K., & Simmonds, I. (2021). Antarctic skin temperature warming related to enhanced downward longwave radiation associated with increased atmospheric advection of moisture and temperature. *Environmental Research Letters*, *16*(6), 064059. https://doi.org/10.1088/1748-9326/ac0211

Silber, I., Verlinde, J., Wang, S.-H., Bromwich, D. H., Fridlind, A. M., Cadeddu, M., et al. (2019). Cloud influence on ERA5 and AMPS surface downwelling longwave radiation biases in West Antarctica. *Journal of Climate*, *32*(22), 7935–7949. https://doi.org/10.1175/jcli-d-19-0149.1

Stillwell, R., Rowe, P., Cordero, R., Zou, X., & Gorodetskaya, I. (2025). Cloud mask data (King George Island), 2017–2023 [Dataset]. *AMRDC Data Repository*. https://doi.org/10.48567/1wd1-ea27

Stillwell, R. A., Neely III, R. R., Thayer, J. P., Shupe, M. D., & Turner, D. D. (2018). Improved cloud-phase determination of low-level liquid and mixed-phase clouds by enhanced polarimetric Lidar. *Atmospheric Measurement Techniques*, *11*(2), 835–859. https://doi.org/10.5194/amt-11-835-2018

Tansey, E., Marchand, R., Alexander, S. P., Klekociuk, A. R., & Protat, A. (2023). Southern Ocean low cloud and precipitation phase observed during the Macquarie Island Cloud and Radiation Experiment (MICRE). *Journal of Geophysical Research*, *128*(17), e2023JD039205. https://doi.org/10.1029/2023JD039205

Trenberth, K. E., & Fasullo, J. T. (2010). Simulation of present-day and twenty-first-century energy budgets of the southern oceans. *Journal of Climate*, *23*(2), 440–453. https://doi.org/10.1175/2009JCLI3152.1

Wang, H., Klekociuk, A. R., French, W. J. R., Alexander, S. P., & Warner, T. A. (2020). Measurements of cloud radiative effect across the Southern Ocean (43°S–79°S, 63°E–158°W). *Atmosphere*, *11*(9), 949. https://doi.org/10.3390/atmos11090949

Wille, J. D., Alexander, S. P., Amory, C., Baiman, R., Barthélemy, L., Bergstrom, D. M., et al. (2024). The extraordinary March 2022 East Antarctica "heat" wave. Part I: Observations and meteorological drivers. *Journal of Climate*, *37*(3), 757–778. https://doi.org/10.1175/jcli-d-23-0175.1

Zhang, Z., Ralph, F. M., Zou, X., Kawzenuk, B., Zheng, M., Gorodetskaya, I. V., et al. (2024). Extending the Center for Western Weather and Water Extremes (CW3E) atmospheric river scale to the Polar Regions. *The Cryosphere*, *18*(11), 5239–5258. https://doi.org/10.5194/tc-18-5239-2024

Zou, X., Rowe, P. M., Gorodetskaya, I., Bromwich, D. H., Lazzara, M. A., Cordero, R. R., et al. (2023). Strong warming over the Antarctic Peninsula during combined Atmospheric River and foehn events: Contribution of shortwave radiation and turbulence. *Journal of Geophysical Research: Atmospheres*, *128*(16), e2022JD038138. https://doi.org/10.1029/2022jd038138